Evaluation of Ionospheric Delay for Moon-Based Repeat-Pass InSAR Based on International Reference Ionosphere Model

Kai Wu ⓘ, Huadong Guo ⓘ, *Member, IEEE*, Guang Liu ⓘ, *Member, IEEE*, Wenjin Wu, Yixing Ding ⓘ, and Guoqiang Chen

Abstract—Moon-based synthetic aperture radar (SAR) offers unprecedented temporal and spatial coverage. Its repeat-pass interferometry is expected to play a substantial role in earth science because of its large-scale, long-term, near 24.8 h revisit period, and stable earth observation ability. However, it faces a greater challenge when the signal passes through the ionosphere compared with the low Earth orbit (LEO) satellite. In this study, we constructed a total electron content (hereafter referred to as TEC) calculation model for the propagation path of a moon-based SAR signal based on International reference ionosphere model and moon-based SAR interferometry (InSAR) geometry. Subsequently, the ionospheric delay at various carrier frequencies was quantitatively evaluated under different time baseline types. The results show that the interferometric phase space gradient caused by ionospheric can reach ten times that of LEO SAR satellites with superposition of diurnal and seasonal ionospheric variations. In addition, this problem in the observation area with a large incident angle is more severe, which limits the effective swath width of moon-based repeat-pass InSAR. The ionospheric delay effects can be avoided to some extent by selecting the interference combination at nighttime or approaching the solar altitude angle. To highlight the large-scale ground deformation information in most cases and give full play to the long-term and stable observation advantages of the moon-based platform, accurate ionospheric correction or compensation must be considered.

Index Terms—Imaging geometry, ionospheric effect, International reference ionosphere (IRI) model, large-scale observation application, moon-based platform, repeat-pass InSAR, signal propagation path, time baseline.

I. INTRODUCTION

I N THE solar-terrestrial system, the flowing electrons and ions in the ionosphere generally have considerable effects on refraction, scattering, and polarization plane rotation when radio waves pass through [1]. Synthetic aperture radar (SAR) technology mainly uses low-frequency electromagnetic wave signals to facilitate Earth observation, and ionospheric effects are particularly significant. Ionospheric delay is one of the most important effects, and comprehensive consideration of this factor is essential in the development of both SAR imaging and SAR interferometry [2].

Artificial satellite InSAR is a space technology that extracts phase information from the complex radar data of a SAR sensor. In recent years, this technology has made substantial contributions in effectively determining the digital elevation model and accurately capturing large-area deformation [3], [4]. It has been successfully applied in seismic deformation measurements, land subsidence, volcanic monitoring, and landslide monitoring [5], [6], [7], [8], [9]. However, for some scientific phenomena on a global scale, the low Earth orbit (LEO) SAR platform is restricted by small swaths and long revisit periods [10], [11], [12]. A new platform with a higher orbit is expected to overcome these limitations, and the global change observation lunar based SAR was proposed by Guo to explore the possibility of a moon-based platform [13]. Some studies on observation geometry have shown that moon-based SAR has unprecedented spatial-temporal coverage, and the development of this technology will bring great potential for global change observation and geoscience cognition [14], [15], [16].

There are three main differences when the signal of the moon-based SAR passes through the ionosphere during interferometry compared with LEO SAR: 1) the altitude of the LEO satellite is in the middle of the earth's ionosphere (65–2000 km), while the microwave of the moon-based SAR will pass through the whole ionosphere; 2) for moon-based SAR, the observation target should pass through the radar beam from west to east, and the earth curvature must be considered to achieve a wider swath; consequently, the ionospheric information in the range direction will change obviously along with the increase of incident angle (IA) [17]; 3) the variation period of the solar altitude angle is approximately 24 h, while the average revisit period of the moon-based SAR is approximately 24.8 h, which does not strictly satisfy the sun-synchronization observation. The ionospheric state difference between the two images of repeat-pass is greater with an increase in the revisit interval. (The moon also has an ionosphere, but its electron content is two
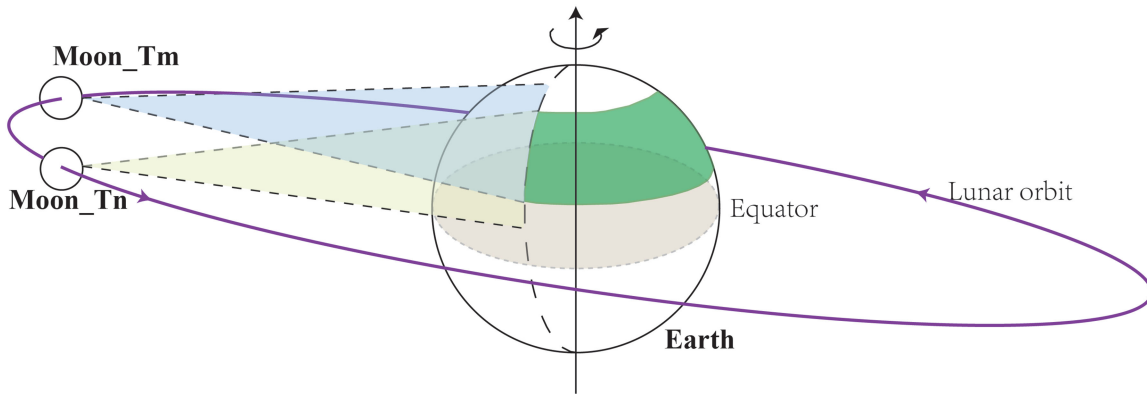
Fig. 1. Observation geometry of moon-based repeat-pass InSAR (not to scale). The relative motion between the moon-based sensor and the observation target is realized by the rotation of the earth and the revolution of the moon. The swath is formed from east to west. The lunar declination is not always the same at different observation times, so the repeat-pass swath of moon-based InSAR is the common area of the two observations (green area in the figure).

orders of magnitude less than that of Earth's ionosphere [18]; the ionosphere in this study only refers to the Earth's ionosphere).

There have been many studies on the evaluation and correction of ionospheric effects for LEO SAR platforms in recent years, including both SAR imaging and SAR interferometry [19], [20], [21], [22], [23], [24]. However, for moon-based SAR, there are still few similar research conclusions as far as we know. At this stage, the evaluation based on an empirical model rather than measured data is also of certain scientific significance, considering that the spatial resolution design of moon-based SAR for global scientific phenomena is commonly lower than LEO SAR. In this study, we evaluated it based on the International reference ionosphere (IRI) model and the observation geometry of moon-based InSAR. The research results can provide a reference for the design of sensors for moon-based SAR platforms in the future.

This study aims to clarify the ionospheric delay of moon-based InSAR through theoretical derivation and model simulation. The remainder of this study is organized as follows: The model and simulation methods are presented in Section II. In Section III, we summarize the spatial and temporal characteristics of the ionosphere and consider them as a calculation reference for the peak delay of moon-based InSAR. Then, we quantitatively evaluated the ionospheric delay at various carrier frequencies under short-time and long-time baseline. In Section IV, we discuss the limitations of ionospheric delay in the application of moon-based InSAR and propose possible correction or compensation ideas. Finally, the conclusions are drawn.

II. GEOMETRIC MODEL AND SIMULATION METHOD

The simulation work of this study is based on accurate geometric model, a diagram of moon-based repeat-pass InSAR is shown in Fig. 1. This part introduces three aspects around how to combine the IRI model with observation geometry: spatial coverage calculation method of precise spatial-temporal reference system, effective interference combination screening, and ionospheric delay calculation method of the signal propagation path. By comparing the ionospheric delay information with
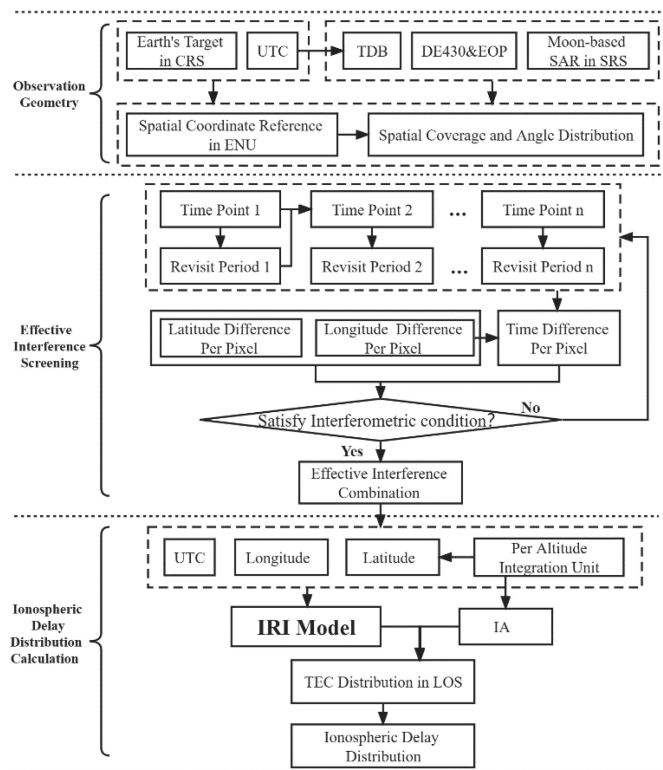
Fig. 2. Ionospheric delay distribution calculation process under various effective interference combinations of moon-based repeat-pass InSAR.

the large-scale deformation in the interferometric phase, the ionospheric correction accuracy goal of various time baseline types can be determined. The specific process is shown in Fig. 2.

A. Observation Geometry and Spatial Coverage of Moon-Based SAR

To establish the geometric relationship between the moon-based SAR system and the target at a certain time, we introduced two time systems and seven coordinate references in this study.

The time system includes universal time coordinated (UTC) and barycentric dynamical time (TDB). The former is used as

Name	Origin	X-axis	Z-axis
MCMF	Moon's center	mean Earth direction	mean rotational pole of Moon
ECEF	Earth's center	Greenwich Meridian	North pole of Earth
SCRS	Moon's center	vernal equinox	the celestial north
GCRS	Earth's center	vernal equinox	the celestial north
ENU	ground station	East of the station	North of the station

an input to the IRI model to obtain the electron concentration distribution, and the latter is used as an input to the ephemeris to obtain lunar position information. The transformation between TDB and UTC is performed as follows:

$$\text{TDB} = \text{UTC} + \Delta t_1 + \Delta t_2 + \Delta t_3 \tag{1}$$

where Δt_1 represents the leap seconds between the UTC and international atomic time (TAI). They are provided by the International Earth Rotation and Reference Systems Service (IERS) which are available online at http://www.iers.org. Δt_2 represents the difference between the TAI and terminal time (TT), which is a constant of 32.184 s. Δt_3 represents the difference between TDB and TT. For the Earth-Moon system, the following approximate formula can satisfy the accuracy requirements [25].

$$\Delta t_3 = 0.001\,657 \sin a + 0.000\,022 \sin\left(L_s - L_j\right) \tag{2}$$

where a, L_s, and L_j represent the mean anomaly, Sun's mean longitude, and Jupiter's mean longitude, respectively. The calculation methods have been described in [26].

In this study, the reference system used can be briefly divided into two categories. The first type is the geodetic reference system, which uses longitude, latitude, and height to indicate the location of the ground point. Two kinds of geodetic reference systems were used in this study, the Earth and Moon correspond to geographic reference system and selenium reference system (SRS), respectively. The second type is the Cartesian coordinate system, which represents the spatial position through three-dimensional (3-D) coordinates. This study mainly involved the moon-centered moon-fixed coordinate system (MCMF), international terrestrial reference system (also known as earth-centered earth-fixed coordinate system, ECEF), geocentric cellular reference system (GCRS), selenium cellular reference system (SCRS), and local Cartesian coordinate system (also known as East-North-Up coordinate system, ENU). All these Cartesian coordinate systems follow the right-hand rule, and their origin and axis directions are listed in Table I.

The spatial coverage simulation of the moon-based SAR in this study was mainly carried out in the coordinate framework of the ENU. When the observation target position and SAR antenna position are determined in the geodetic reference system, we can calculate the distance vector $\boldsymbol{L}$ (see Fig. 3) at any time in the ENU coordinate system. The transformations of all the above coordinate systems are shown in Appendix A. In this study, an ENU coordinate system is established for each ground position, which can avoid complex spherical angle calculations and be easier to understand compared to the simulation in ECEF framework.
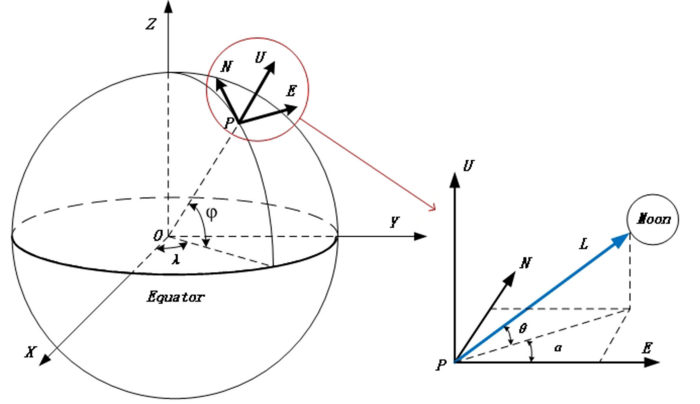

Fig. 3. ENU and ECEF coordinate framework. The ENU direction can be obtained by rotating a "90+λ" angle counterclockwise along the Z-axis and then rotating a "90-φ" counterclockwise around the X-axis from ECEF.

The spatial coverage of SAR system is closely related to the IA and azimuthal angle (AA). When the distance vector in the ENU framework at position P (λ, φ, H_0) is determined as $\boldsymbol{L}$ (L_E, L_N, L_U), the observation AA of moon-based SAR at P can be expressed as (ranging from 0° to 180°)

$$\alpha = \begin{cases} \tan^{-1}\left(|L_N|/L_E\right), & L_E > 0 \\ \tan^{-1}\left(|L_N|/L_E\right) + 180°, & L_E < 0 \\ 90°, & L_E = 0 \end{cases} \tag{3}$$

The observation elevation angle of the moon-based SAR at P can be expressed as

$$\theta = \begin{cases} 90°, & L_N^2 + L_E^2 = 0 \\ \cos^{-1}\left(L_U/\sqrt{L_N^2 + L_E^2}\right), & L_N^2 + L_E^2 \neq 0 \end{cases} \tag{4}$$

When $\theta > 0$, the moon-based SAR and observation targets are intervisible, and the corresponding region is approximately half of the Earth's surface. In this case, the IA of the signal varies from 0° to 90°, and can be expressed as

$$\text{IA} = 90° - \theta. \tag{5}$$

It is difficult to ensure imaging quality of SAR systems in the area near the nadir point owing to the echo ambiguity. Moreover, the area with a large IA will put forward higher requirements for the transmission power of the SAR antenna. Thus, IA should have a reasonable range. The IA of LEO SAR is usually limited within a range of 20°–60°. Considering the effective coverage of moon-based SAR in the polar and equatorial regions [27], the IA range will be set at 15°–75° for subsequent simulations.

Fig. 4 has shown the simulation of instantaneous coverage taking AA range of 45°–135° and June 15, 2020, 0:00 as an example. The range between the black dashed lines corresponds to the effective swath of moon-based SAR during the scanning process. The north and south parts correspond to right-looking and left-looking areas, respectively, and the swath width on each side can exceed 6000 km in this IA range. It is very important to compensate the variation of Doppler centroid for SAR imaging quality, because the non-zero Doppler centroid can cause significant errors during azimuth compression and geolocation [28], [29]. After certain zero Doppler steering control, the zero
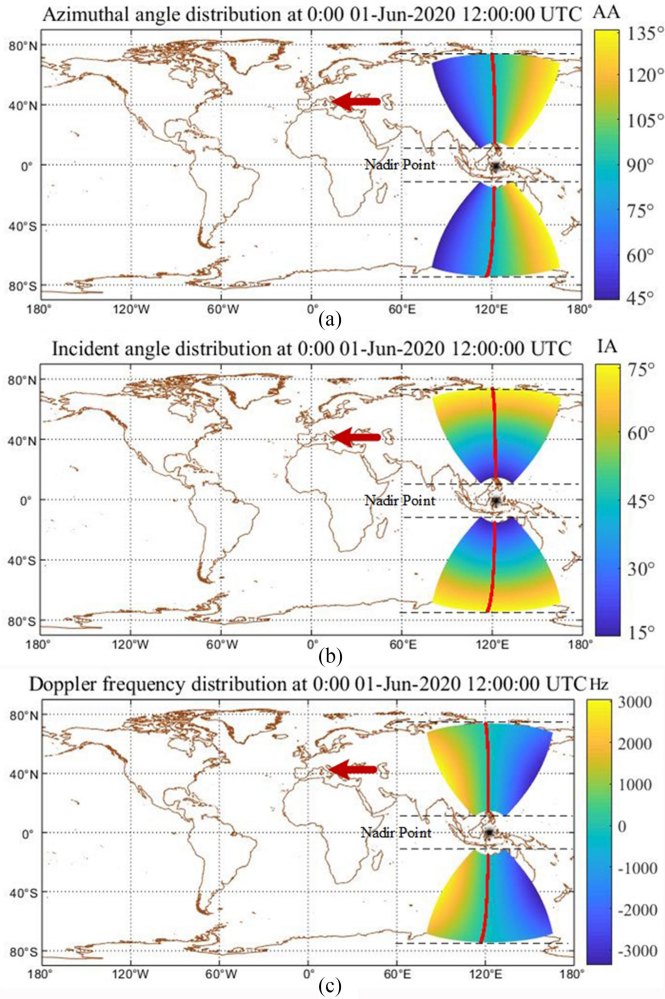
Fig. 4. Instantaneous distribution of (a) AA, (b) IA, and (c) Doppler frequency for moon-based SAR.

Fig. 5. Lunar declination and the expected variation of the nadir point's next revisit (take June, July, and August of 2019 as an example).

Doppler line (the red line in Fig. 4) will shift in a longitude direction. The Doppler frequency f_{Doppler} of a ground target is given by [30]

$$f_{\text{Doppler}} = -\frac{2}{\lambda} \frac{\boldsymbol{L} \cdot (\boldsymbol{V_{SAR}} - \boldsymbol{V_P})}{|\boldsymbol{L}|} \qquad (6)$$

where λ is the radar wavelength; $\boldsymbol{V_{SAR}}$ and $\boldsymbol{V_P}$ are the velocity vectors of the moon-based SAR system and ground target, respectively.

B. Ionospheric Delay Evaluation Method of the Moon-Based InSAR

Compared with the LEO SAR platform, it is quite different in the timing selection (t_1, t_2) of master image and slave image for moon-based InSAR. This is because the operation of the moon-based platform depends on the trajectory of the natural satellite, which is more stable but uncontrollable. InSAR technology has strict requirements for the attributes of master and slave images. The quality of interferograms is closely related to the baseline length and angle difference [31]. LEO SAR always uses fixed AA and IA in the same observation area to acquire data and
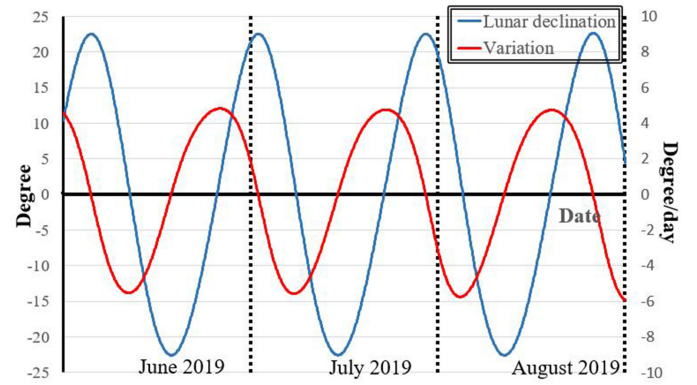
generate images. Due to the extraordinarily large observation range and unique orbit of moon-based SAR, the difference of IA and AA in SAR images is more complex. Generally, the spatial decorrelation is mainly related to IA. The IAs are determined by the latitude difference between the target and nadir point [see Fig. 4(b)], and the change rule of nadir point is consistent with lunar declination [10], [14]. We use Fig. 5 to reveal the timing selection method for an effective interference combination.

The blue and red lines in Fig. 5 represent the lunar declination and expected variation, respectively. A revisit of the nadir point is the minimum time difference when two nadir points are located at the same longitude. A larger absolute value of lunar declination corresponds to a smaller absolute value of variation. The variation value is in the range of -5°–5°. If we want the time baseline of the interference simulation to be of the order of days, we must select the time points corresponding to the larger absolute value of lunar declination. This can ensure that the lunar declination is relatively close in these days, and the IAs of the observation target is close. If we want the time baseline of interference simulation to be of the order of months, all time points can be selected, but they need to be screened by quantitative calculation of IA

$$\left| \sin \left(\frac{\beta_{t1} - \beta_{t2}}{2} \right) \right| < \tan \left(\frac{\beta_{t1} + \beta_{t2}}{2} \right) \frac{B}{2f} \qquad (7)$$

where B is the signal bandwidth and β_{t1} and β_{t2} are the IAs corresponding to time points t_1 and t_2. LEO SAR usually uses a critical baseline to evaluate interference quality, but it is not suitable for moon-based SAR. The main reason is that the height of the moon-based orbit varies in the range of about 363 300–405 500 km, and some geometric approximations for the critical baseline may cause errors. Formula (7) is derived from the overlap of the echo spectrum information without any observation angle and average slant range approximation (see Appendix B for the specific derivation process). Meanwhile, after zero Doppler steering control, a baseline along the azimuth direction will be generated at different revisit times. In order to avoid this negative effect, the revisit period used in this study is defined as the time period when the zero Doppler steering returns to the same position.

We calculated the long-time series of lunar declination changes to ensure the efficiency of effective interference screening. The revisit type was further classified according to the revisit period length as well as the temporal variation characteristics of ionosphere. The delay between the selected master image and slave image corresponded to the change of total electron content (TEC) in the LOS. The longitude and latitude density of the distribution results is 0.1°. The TEC simulation of each pixel is the mean value in synthetic aperture time (100 s is used in this study).

C. Simulation Method of Signal Propagation Path for Moon-Based SAR in Ionosphere

The IRI model is an international project that provides the electron density, electron temperature, ion temperature, and ion composition (O+, H+, He+, N+, NO+, O2+, and cluster ions) in the ionospheric altitude range (65–2000 km for the daytime and 80–2000 km for the nighttime) for a given location, time, and date. This model and the corresponding software are continuously updated, which is available at https://ccmc.gsfc.nasa.gov/modelweb/models/iri2016_vitmo.php. The mass of a single free electron in the ionosphere is significantly smaller than that of a single ion. It is generally considered that electrons play a dominant role in the ionosphere. The study of the ionospheric effect on microwaves is usually based on the density of free electrons, which is a function of Sun's activity, atmospheric density profile, magnitude, and orientation of the Earth's magnetic field. There are significant differences in the generation, disappearance, and migration of free electrons in different regions, which makes the ionosphere anisotropic [32]. The spatial variation of vertical total electron content (VTEC) is an important reference index in the study of ionospheric effects of LEO SAR [33]. And some studies have considered the IA of SAR and introduced the slant total electron content (STEC) [34], [35].

If only the VTEC model is used, the ionosphere is often regarded as a layer without thickness. Correspondingly, if the STEC model is used, the ionosphere is often regarded as a homogeneous layer of a certain thickness. To reflect the TEC in the line-of-sight (LOS) direction more accurately, we regard the ionosphere as a multiple-layer structure, and the TEC is an integral of different heights, thicknesses, and IAs. The TEC in the LOS of the moon-based Earth observation geometry is shown in Fig. 6.

The azimuth resolution of a spaceborne SAR is proportional to the synthetic aperture [36], and the synthetic aperture time of moon-based SAR is much longer than that of LEO SAR to achieve a certain azimuth resolution. In this study, the following assumptions were made.

1) The ionosphere is divided into multiple layers along the normal direction with the reference ellipsoid, and each layer is uniform in one height integration unit.
2) The distribution of ionospheric electrons in the horizontal direction is anisotropic, but uniform in each pixel unit.
3) In one synthetic aperture time for moon-based SAR (on the order of tens to hundreds of seconds [37], [38]), the
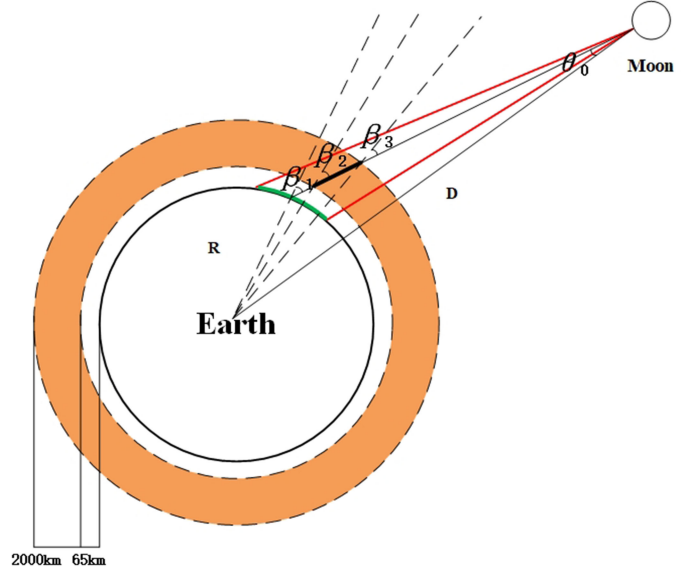

Fig. 6. TEC in LOS on the propagation path of moon-based SAR signal (Zero Doppler plane).

electron density in the scanning area remains time-invariant. This assumption can only be used in interferometric delay analysis. For the moon-based SAR imaging analysis, the results need to be compensated.

Fig. 6 has shown the signal path in the zero Doppler plane. R represents the radius of the earth, D represents the distance between the Earth's center and the moon-based sensor, θ_0 represents the lunar off-line angle for the signal, while β_1, β_2, and β_3 represent the IA of the signal passing through the ground, bottom of the ionosphere, and top of the ionosphere, respectively. The orange area represents the ionosphere, the thick green line represents the ground swath, and the thick black line represents the complete path of the signal through the ionosphere. The following triangular relationships exist in the geometry described above:

$$\begin{cases} D/\sin\beta_1 = R/\sin\theta_0 \\ D/\sin\beta_h = (R+h)/\sin\theta_0 \end{cases} \tag{8}$$

where h is the height of the ionosphere (65–2000 km) and β_h is the IA at a height of h. Based on (8), β_h and θ_0 can be derived as

$$\beta_h = \sin^{-1}\left(\frac{R\sin\beta_1}{R+h}\right) \tag{9}$$

$$\theta_0 = \sin^{-1}\left(\frac{R\sin\beta_1}{D}\right)$$

$$= \sin^{-1}\left(\frac{R\sin\beta_1}{\left|\boldsymbol{P}_{\text{SAR}}^{\text{GCRS}}\right|}\right)$$

$$= \sin^{-1}\left(\frac{R\sin\beta_1}{\left|[R_Z][R_X][R_Z]\boldsymbol{P}_{\text{SAR}}^{\text{MCMF}} + \boldsymbol{P}_{\text{Moon}}^{\text{GCRS}}\right|}\right) \tag{10}$$

where $\boldsymbol{P}_{\text{SAR}}^{\text{GCRS}}$, $\boldsymbol{P}_{\text{SAR}}^{\text{MCMF}}$, and $\boldsymbol{P}_{\text{Moon}}^{\text{GCRS}}$ represent the vector of SAR antenna or lunar center in the corresponding coordinate system.

$P_{\text{Moon}}^{\text{GCRS}}$ and rotation matrix $[R_Z][R_X][R_Z]$ are extracted from ephemeris data. $P_{\text{SAR}}^{\text{MCMF}}$ is related to the longitude and latitude of SAR antenna on the lunar surface (see Appendix A). When the IA of the scanning area was 50°, the IA at the bottom of the ionosphere (65 km) was approximately 49.3°, and the IA at the top of the ionosphere (2000 km) was approximately 35.7°. It is certain that the IA of the signal varies throughout the ionosphere for moon-based SAR, so it is necessary to use (11) to calculate the TEC

$$\text{TEC}_{\text{LOS}} = \int_{65}^{2000} n_e(h) \sec(\beta_h) dh$$
$$\approx \sum_{i=1}^{388} 5000 n_e(60 + 5i) \sec\left(\sin^{-1}\left(\frac{R \sin \beta_1}{R + h}\right)\right). \tag{11}$$

Here, TEC_{LOS} is defined as the number of free electrons in a tube with a 1-m^2 cross section along the signal propagation path. And $n_e(h)$ represents the number of free electrons in a cubic with a 1-m^3 at a height of h, which can be extracted from IRI model. (In this study, it is called every 5-kilometer height, which is sufficient to meet the simulation requirements). The whole path covers different longitudes and latitudes. It is also necessary to obtain the exact location $(\text{lon}_h, \text{lat}_h)$ based on the longitude and latitude difference with the nadir point

$$\text{lon}_h = \text{lon}_{\text{nadir}} - (\beta_h - \theta_0)\cos(\alpha) \tag{12}$$
$$\text{lat}_h = \text{lat}_{\text{nadir}} \pm (\beta_h - \theta_0)\cos(|\alpha - 90|). \tag{13}$$

The $(\text{lon}_{\text{nadir}}, \text{lat}_{\text{nadir}})$ can be derived from $P_{\text{SAR}}^{\text{ECEF}}$ (see Appendix A). The α is ground AA before zero Doppler steering control, which is also location dependent (see Fig. 4). Therefore, the final result needs to be determined through iteration.

When the ionized gas is regarded as a perfect dielectric, its refractive index for a radar wave of frequency f is given by

$$n_{\text{iono}} = 1 - K n_e / f^2 \tag{14}$$

where $K = 40.28 \ (\text{m}^3/\text{s}^2)$, the deviation of the ionospheric refractive index is relatively small; thus, the scaled-up "refractivity" N_{iono} is often used

$$N_{\text{iono}} = (n_{\text{iono}} - 1) \cdot 10^6 = -K \cdot 10^6 n_e / f^2. \tag{15}$$

For a low-frequency SAR system, when the modulation code signal and phase signal pass through the ionosphere, they will experience group path and phase path, which will cause group delay and phase advance respectively. The two paths are equal in magnitude but opposite in sign [21]

$$I_g = -I_p = -10^{-6} \int N_{\text{iono}} dl \tag{16}$$

where l is the signal propagation path. The group delay is usually characterized by time. According to (11), (15), and (16), the ionospheric group delay is inversely proportional to the square of the signal frequency and directly proportional to the TEC as (one-way travel):

$$I_{g,t} = K \cdot \text{TEC}_{\text{LOS}} / c f^2 \tag{17}$$

where c is the speed of light.

The time delay will cause location error, but it can be effectively eliminated in the process of complex image coregistration. InSAR technology mainly uses phase information, the difference between two phase advances is the focus of this study on the ionospheric delay effect. The difference of TEC in LOS at pixel k from t_1 to t_2 corresponds to

$$\delta \, \text{TEC}_{\text{LOS},k}^{t1,t2} = \text{TEC}_{\text{LOS},k}^{t1} - \text{TEC}_{\text{LOS},k}^{t2}. \tag{18}$$

The ionosphere-induced true interferometric phase at pixel k from t_1 to t_2 corresponds to (two-way travel)

$$\delta \, \varphi_k = \delta I_g \cdot 4\pi / \lambda = 4 K \pi \cdot \delta \text{TEC}_{\text{LOS},k}^{t1,t2} / cf. \tag{19}$$

III. SIMULATION RESULTS AND ANALYSES

The layered structure of the ionosphere is composed of both regularities and irregularities. The regularities part is also called the background ionosphere, which corresponds to most areas observed by moon-based SAR. Ionospheric irregularities are formed mainly due to the instability of the ionospheric E and F layers, resulting in a change in electron density relative to the background ionosphere. Some studies have shown that, although ionospheric irregularities are mainly distributed in specific regions (such as the polar region, and the equatorial region of Atlantic-Africa), their contributions to scattering and dispersion can far exceed the background ionosphere. In this section, we discussed the spatial and temporal characteristics of the background ionosphere and irregularity region through the global distribution of VTEC, which can be used as a reference for the calculation of peak delay. Then, the ionospheric delay of the moon-based InSAR were evaluated under short-time and long-time baselines, respectively.

A. Spatial and Temporal Characteristics of the Background Ionosphere

Regardless of the solar activity, the position of sunlight can dominate the change in the background ionosphere. Taking 2019 as an example, Fig. 7 has shown the global VTEC distribution during the spring equinox (autumnal equinox is similar), summer solstice, and winter solstice. On these specific dates, the Sun is over the equator, the Tropic of Cancer, and the Tropic of Capricorn.

The ionospheric electron concentration is related to the terminator line in Fig. 7, and the VTEC during the daytime is much higher than that at night. We calculated the electron density profiles along the altitudes of the daytime and the nighttime regions in 2019 to illustrate the spatial differences in the ionosphere. We also calculated the 48 h VTEC variation in the global region to illustrate the temporal differences in the ionosphere. Fig. 8 has shown these differences by taking a specific date and a specific location as examples.

As shown in Figs. 7 and 8(b), the ionospheric state is related to the solar altitude angle. This correlation can be used to select the moon-based SAR interferometric combination for peak ionospheric delay. The statistical results in 2019 have shown that it can reach 60 times more for VTEC in the daytime region than in the nighttime region on a specific day, and the
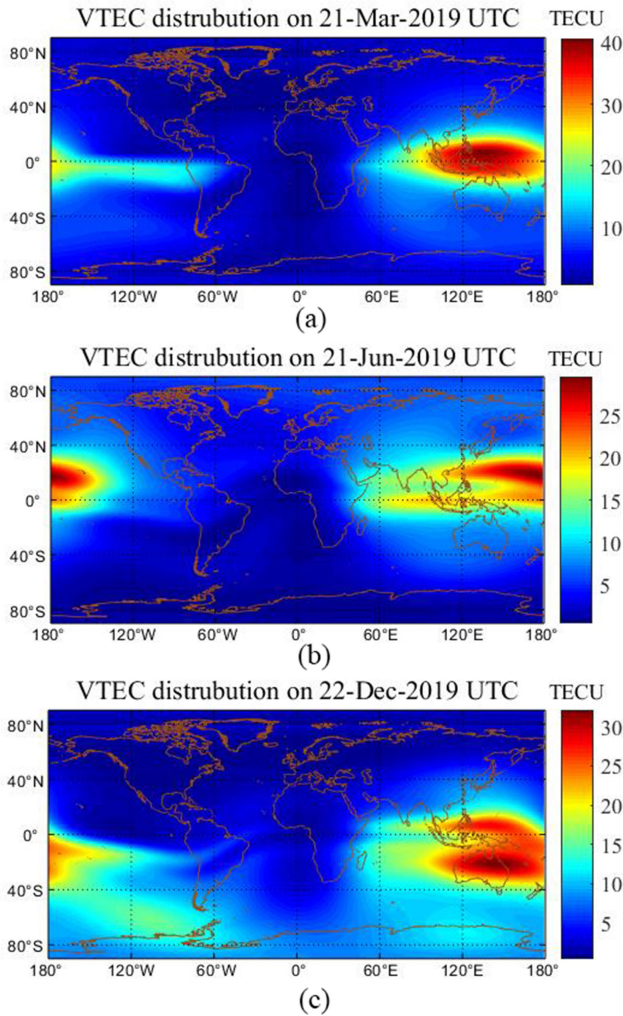
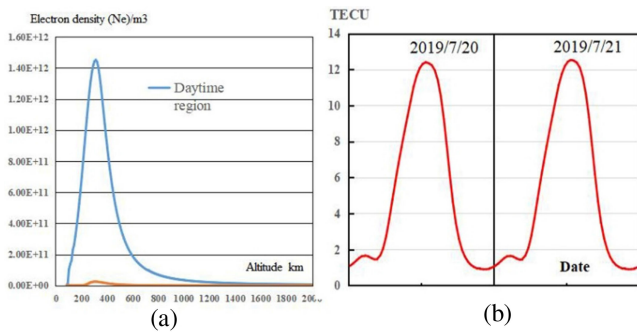Fig. 7. Global distribution of VTEC in (a) Spring equinox, (b) Summer solstice, and (c) Winter solstice.

Fig. 8. (a) Comparison between daytime region and nighttime region on spring equinox of 2019. (b) VTEC variation from 2019/7/20 to 2019/7/21 at the position (35 °S, 65 °W).

maximum value of VTEC in the short term can reach 10–20 times more than the minimum value at a specific position. The worldwide flow of irregularities is the main reason why the spatial correlation between VTEC and solar altitude angle is lower than the temporal correlation. We believe that if there are no irregularities flow in a region (the background ionosphere is
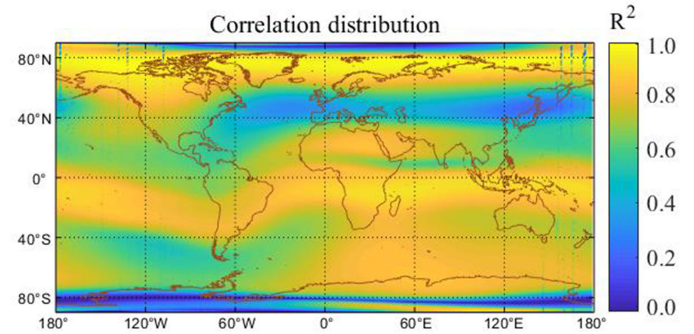

Fig. 9. Regression analysis of solar altitude angle and VTEC in global region from 2019/7/20 to 2019/7/21.

dominant), the variation of the solar altitude angle and VTEC will show a higher correlation.

Before the moon-based InSAR simulation, we used the results of the short-term regression analysis of VTEC and solar altitude angle as a reference for the selection of the time baseline corresponding to peak delay. Taking 2019/7/20–2019/7/21 as an example, Fig. 9 has shown the global distribution of their correlation coefficients. The regions with the lower value of R^2 should have more irregularity flow.

The phase screen theory can simulate the scintillation effect caused by ionospheric irregularity to a certain extent, which is the main fashion to study ionospheric scintillation [38]. However, the theory has some premises, such as phase disturbance of Gaussian stochastic distribution, frozen field, and isotropy. Under the strong fluctuation of ionospheric scintillation, more constraints are needed to obtain the solution of the model. As a large-scale evaluation work, we focus on the flexible time baseline of moon-based SAR and the 3-D simulation ability of the IRI model. Therefore, the regression analysis results are used as a reference in this study, and it is enough to support the conclusion of the magnitude of ionospheric delay.

With a change in solar activity, the ionospheric state has an 11-year period. The year 2019 simulated in this study corresponds to the solar activity valley, and the ionospheric electron content in the peak year can reach 20 times that in 2019 (such as 1958). The ionospheric delay in other years can amplify the results of this study to a specific scale.

In a moon-based SAR image, the observation local time of different areas is relatively close, because it is only about 0.8 h different from the solar altitude angle period. The following preliminary conclusions can be drawn from the above analysis:

1) If the effective interference region is nighttime for two-time points with the less irregularity flow, the variation of the ionospheric state is relatively small for both long-time baseline and short-time baseline of moon-based SAR.

2) The short-time baseline of the moon-based SAR is mainly affected by diurnal variation of the ionosphere. The time baseline corresponding to the maximum ionospheric delay is related to the time point at which the diurnal change rate is the highest, which is approximately 11:00–13:00 local time, as shown in Fig. 8(b).

TABLE II
TIME INTERVALS CORRESPONDING TO EFFECTIVE INTERFERENCE
OF SHORT-TIME BASELINE

Time interval in 2019	
2019/01/03–2019/01/08	2019/07/13–2019/07/18
2019/01/18–2019/01/21	2019/07/28–2019/08/01
2019/01/30–2019/02/04	2019/08/09–2019/08/14
2019/02/14–2019/02/18	2019/08/24–2019/08/28
2019/02/26–2019/03/03	2019/09/05–2019/09/11
2019/03/13–2019/03/17	2019/09/20–2019/09/25
2019/03/26–2019/03/31	2019/10/03–2019/10/08
2019/04/09–2019/04/14	2019/10/17–2019/10/22
2019/04/22–2019/04/27	2019/10/30–2019/11/04
2019/05/07–2019/05/11	2019/11/14–2019/11/18
2019/05/19–2019/05/24	2019/11/27–2019/12/02
2019/06/03–2019/06/07	2019/12/11–2019/12/16
2019/06/16–2019/06/21	2019/12/24–2019/12/29
2019/06/30–2019/07/05	

Fig. 10.   Simulation results of maximum delay of short-time baseline in 2019.

3) The long-time baseline of moon-based SAR is affected not only by diurnal variation of the ionosphere but also by seasonal variation. If these two effects can offset each other, the time baseline corresponding to a relatively small ionospheric delay can also be obtained. In this case, the distribution of the solar altitude angle at the two observation times must be similar and have fewer irregularities. However, for the most part, the two effects are superimposed, and the time baseline corresponding to the maximum ionospheric delay is equivalent to two observation time points: nighttime with fewer irregularities and daytime with maximum solar altitude.

B. Ionospheric Delay Simulation Results for Short-Time Baseline (Several Days)

For the short-time baseline of the moon-based SAR, the observation time with a high absolute value of lunar declination must be selected to meet the requirements of an effective interference combination. We calculated 27-time intervals in 2019 for the interference delay simulation; the specific time intervals are listed in Table II.

InSAR technology obtains the wrapped phase. Although the wrapped phase cannot reflect the absolute phase part, it can reflect phase spatial gradient information caused by ionospheric delay. Therefore, the main purpose of calculating the TEC variation is to simulate this gradient feature. After comparing the ionospheric delay in these time intervals, we found that the maximum ionospheric delay occurred in July 2019, which was mainly affected by abundant irregularities. Fig. 10 has shown the simulation results of TEC variation (10.a) in the LOS and its gradient (10.b) between 2019/7/3 and 2019/7/4. The nadir point was from 11:24 A.M. to 01:26 P.M. local time.
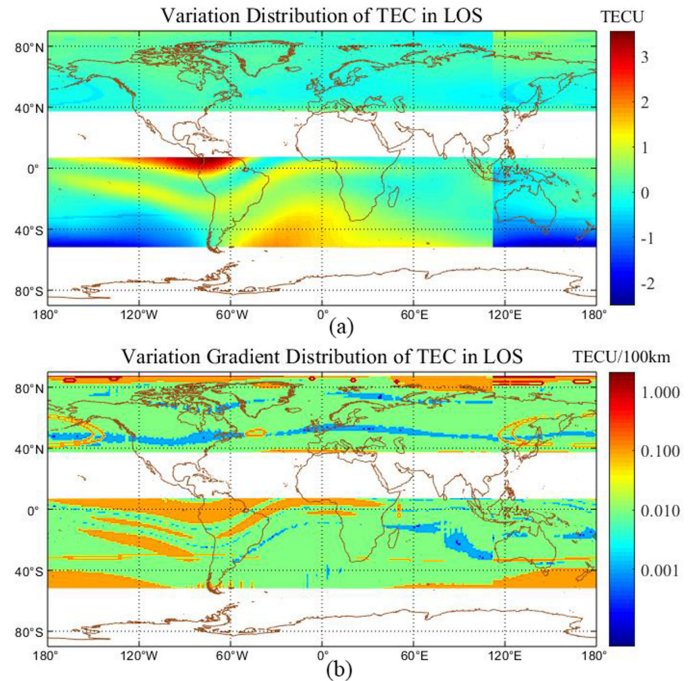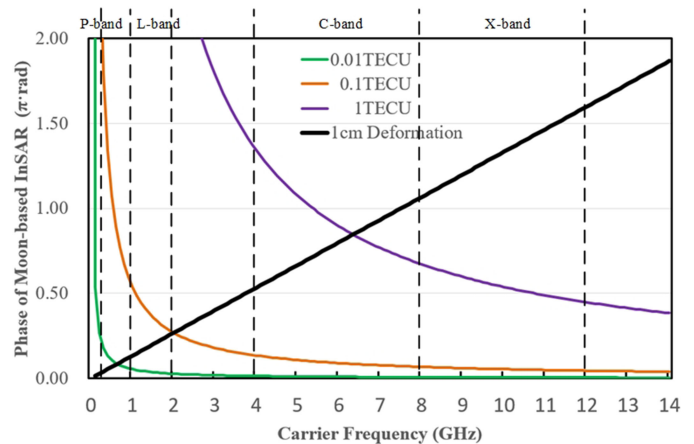

Fig. 11.   Change of ionospheric phase (0.01TECU, 0.1TECU, and 1TECU) and deformation phase (1 cm) with carrier frequency.

The TEC variation in the LOS can reach 3 TECU, and the variation gradient in most areas is 0.01 TECU/100 km. These values increased by one order of magnitude for other years with higher solar activity. Fig. 11 has shown the relationship between the ionospheric delay and deformation phases of the moon-based SAR.

Moon-based InSAR with the repeat-pass mode is mainly used for solid earth deformation types on a global scale [13], [39]. The deformation difference of global scale type within 100 km is always centimeter level [40], [41]. For example, the maximum deformation gradient of solid earth tides is in the range of 0.8–2 cm/100 km [42]. These deformations are characterized by a large range and a small gradient. Taking the deformation of 1 cm/100 km as an example, we compared it with the ionospheric delay.
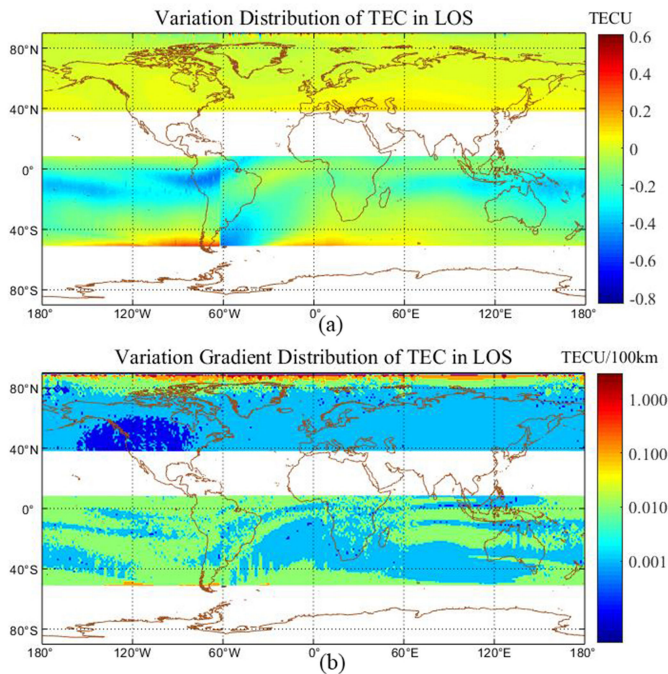
Fig. 12. Simulation results of minimum delay of short-time baseline in 2019.

Fig. 13. Simulation results of maximum superposition delay of long-time baseline in 2019.

The deformation information in the interferogram is equivalent to that of a random ionospheric delay, and this deformation type cannot be extracted when their phases are of the same order of magnitude.

In 2019, there were 8-time intervals at which all observation areas were at night, which corresponded to the minimum ionospheric delay of the short-time baseline. Fig. 12 has shown the simulation results of TEC variation (12.a) in the LOS and its gradient (12.b) between 2019/12/13 and 2019/12/14. The nadir point is from 11:48 P.M. to 01:42 A.M. local time.

For the short-time baseline, if the variation gradient of TEC in the LOS reaches 1 TECU/100 km, the X-band, C-band, L-band, and P-band (common carrier for SAR technology) cannot be used to extract centimeter-level wide-area deformation types. Low-frequency signals are often considered the preferred carriers for moon-based InSAR to achieve more effective spatial coverage [14]. We can obtain the effective interference combination of short-time baseline through the screening of solar activity valley years and time intervals with night areas. However, it is difficult to fully exploit the advantages of the long-term observation of moon-based InSAR. The ionospheric correction or compensation accuracy must reach at least 0.01TECU, or even 0.001TECU for specific deformation types if the L-band short-time baseline InSAR is to be used for long-term observation.

C. Ionospheric Delay Simulation Results for Long-Time Baseline (Several Months)

For the long-time baseline, if the time intervals in Table II are selected, the time baseline of the effective interference combination unit is approximately 22–33 days. There are two
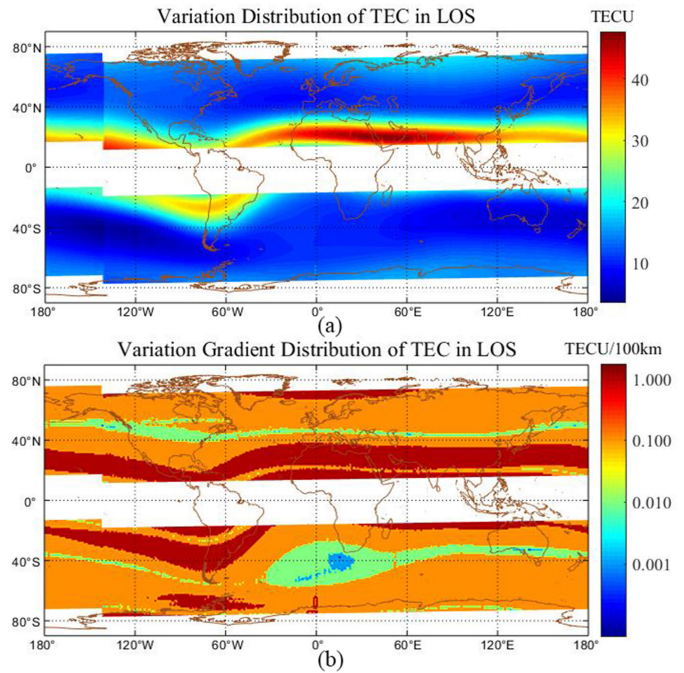
types of time baselines at other time intervals: one is the stable effective interference combination unit, which is approximately 27.3 days, and the other is similar to the ascending-orbit and descending-orbit data of LEO SAR, which are usually less than 13.7 days (refer to Fig. 5). Since the orbital inclination of the second type is close, whether effective interference can be carried out needs special angle evaluation. This study did not explore this issue; therefore, the first stable type was primarily used.

The time baseline with the superposition of diurnal and seasonal variations must be specified to simulate the maximum ionospheric delay. We selected a time point when the observation area was at the maximum solar altitude angle and then screened the nighttime area according to the effective interference. Fig.13 has shown the simulation results of TEC variation (13.a) in the LOS and its gradient (13.b) between 2019/3/21 and 2019/9/28. The nadir point of the former is from 00:32 A.M. to 01:25 A.M. local time, while that of the latter is from 00:04 P.M. to 00:57 P.M. local time.

The TEC variation in the LOS can reach 48 TECU, and the variation gradient in most areas is 0.1 TECU/100 km. In this case, large-scale deformation types could not be effectively observed. General small-scale deformation is also difficult to observe in most areas, because the ionospheric delay is ten times that of the LEO SAR satellites. Although the IRI model cannot accurately reflect small-scale electron distribution, this conclusion can also be obtained from the degree of global delay.

We simulated the time baseline with the offset of diurnal and seasonal variations using the distribution of the solar altitude angle. Fig.14 has shown the simulation results of TEC variation (14.a) in the LOS and its gradient (14.b) between 2019/3/8 and
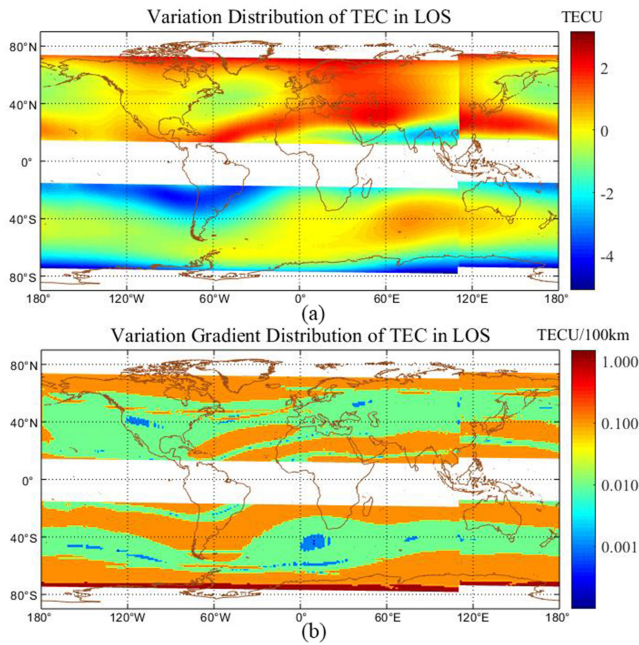
Fig. 14.   Simulation results of maximum offset delay of long-time baseline in 2019.

2019/4/4. The nadir point of the former is from 01:20 A.M. to 02:02 A.M. local time, while that of the latter is from 11:20 A.M. to 00:02 P.M. local time.

Owing to the different seasonal variation rules in the northern and southern hemispheres, only one hemisphere can be considered as the maximum offset area. In this way, the ionospheric delay can be controlled close to the situation in Fig. 10.

For the long-time baseline, the ionospheric delay in the region with a large IA is highlighted, which will narrow the effective interferometry swath. If the L-band long-time baseline InSAR is to be used, the screening of interference combinations cannot achieve the purpose; therefore, accurate ionospheric correction or compensation must be carried out.

IV. DISCUSSION

Moon-based Earth observation is still in the stage of observation theory research, so it is necessary to demonstrate the feasibility of this technology in the future from all aspects. The ionospheric effect is a relatively large problem when moon-based InSAR is applied to solid earth observations. We have performed a quantitative evaluation of this in the study. The ionosphere can also cause other effects such as Faraday rotation and azimuth shifts. These effects need to be considered in imaging processing, which can be ignored in most phase analysis for interferometry simulations. Some experiments show that the phase coherence is reduced when the Faraday rotation angle changes between successive data acquisitions [24]. However, we believe that, compared with the delay effect, it can recover from these effects by satisfying lower ionospheric estimation accuracy.

For a SAR system with a long synthetic aperture time, the ionospheric space-variant law within an azimuth aperture should

be considered. However, for moon-based SAR, we believe that its ionospheric space state is relatively consistent in synthetic aperture time or short-term continuous observation. Because the difference between the period of moon-based SAR and ionospheric change is only about 0.8 h per day, and the variation direction of solar radiation is the same as that of moon-based SAR' nadir point. This can also be understood as the offset of time-variant and space-variant ionosphere. The simulation results in Section III have demonstrated that the ionospheric phase has a relatively small gradient in the azimuthal direction. Using this feature, it may be possible to distinguish the ionospheric phase from the large-scale deformation phase of solid earth. This is because the distribution gradient or texture of the deformation phase is quite different. Moon-based SAR can provide full play to the advantages of time resolution with short-time baseline observation. There are approximately 27 ideal time intervals per year. This can provide a reference for the start-up time of moon-Based SAR in different seasons: when the lunar declination reaches its maximum, the right-looking image can observe the Arctic region, and the left-looking image can be used to observe the equatorial region; when the lunar declination reaches its minimum, the left-looking image can be used to observe the Antarctic region, and the right-looking image can observe the equatorial region. In both cases, the observation regions correspond to more ionospheric irregularities, which brings challenges in the extraction of solid earth deformation information. However, in another way, the perspective of moon-based SAR can cover the most complete irregularities. If moon-based SAR can successfully develop ionospheric correction methods such as LEO SAR's split-spectrum, rang/azimuth sub-bands, and multiple-aperture [20], [43], [44], it may be the most effective means of observing ionospheric irregularities. Various methods have high requirements for coherence of the SAR images, therefore, it is necessary to preprocess the images based on the observation geometry and try to eliminate the decorrelation caused by the ionosphere. On this basis, the ionospheric correction methods of moon-based InSAR can be developed in combination with traditional methods.

InSAR technology obtains deformation information by extracting the phase difference, which is not entirely the relative phase change at the two-time points. Even if there is a same-sized phase change in the entire observation region, this phase change will not affect the deformation extraction, because it is eliminated in the phase unwrapping process. Therefore, the difference in the horizontal distribution of the phase change is the main factor affecting the accuracy of deformation extraction. In a similar example, professional singers can accurately match the pitch with the notes of a song, while amateurs may not be able to do that, but they can let others know which song it is, through rhythm. The interferogram is equivalent to the "rhythm" of phase change, as long as we know the "pitch" of some positions, we can obtain the "pitch" of the whole region according to the interferogram. The deformation error of the interferogram comes from the accuracy of "rhythm," that is, the phase gradient of the observation region. Therefore, the decisive factor of ionospheric delay limiting the application of moon-based InSAR is the horizontal gradient of phase change.

Moon-based repeat-pass InSAR applications are mainly aimed at large-scale solid earth observations, such as solid earth tides, plate boundary displacement, and glacial isostatic adjustment. These global-scale deformation types exhibit the characteristics of a small gradient or a slow change. Moreover, moon-based SAR is likely to use low-frequency signals to design SAR systems to meet interferometry requirements. The effective extraction of deformation information from the interference phase is a great challenge. Therefore, in order to give full play to the advantages of moon-based SAR, it is necessary to obtain accurate ionosphere data and correct or compensate for the delay through an observation geometric model.

V. CONCLUSION

In this study, we quantitatively evaluate the ionospheric delay of a moon-based repeat-pass InSAR based on the IRI model. According to the interferometric geometry, the numerical simulation results of the short-time and long-time baselines are given. Ionospheric delay can be avoided, to some extent, by screening the interference combination. However, in order to realize long-term stable observation of large-scale deformation, we must face the challenge of ionospheric delay correction or compensation. The conclusion obtained in this study is enough to provide a reference for the moon-based SAR system with a synthetic aperture time of 100-s level. If the synthetic aperture time reaches kilo-second level or higher, a more accurate model needs to be developed to take into account the time-variant effects of the ionosphere.

In future work, we will conduct more in-depth theoretical studies on moon-based Earth observation, and it is necessary to enrich the research on sensor and system design. We anticipate that additional research results on moon-based SAR imaging as well as other high-orbit SAR systems will be obtained, which will promote the development and applications of wide-area observation technology, and the understanding of Earth science.

APPENDIX A
TRANSFORMATIONS OF SEVEN COORDINATE REFERENCES

The transformation between the geodetic and Cartesian coordinate systems is to establish the relationship between the longitude-latitude-height and the 3-D coordinate vectors, and the most closely related is the earth-fixed coordinate system [45]. Taking the Earth as an example, if the longitude, latitude, and height are known

$$\begin{bmatrix} X_{ECEF} \\ Y_{ECEF} \\ Z_{ECEF} \end{bmatrix} = \begin{bmatrix} (N_E + h)\cos\phi_{GRS}\cos\psi_{GRS} \\ (N_E + h)\cos\phi_{GRS}\sin\psi_{GRS} \\ ((1 - e^2)N_E + h)\sin\phi_{GRS} \end{bmatrix} \quad (A1)$$

where ψ_{GRS}, ϕ_{GRS}, and h represent longitude, latitude, and height, respectively. N_E represents the curvature radius of reference ellipsoid' prime vertical circle. e represents the oblateness of the Earth. Conversely, if the coordinates in ECEF are known, when $h \gg N_E$, the latitude can be obtained by ($X_{ECEF}^2 + Y_{ECEF}^2 \neq 0$):

$$\phi_{GRS} = \arctan(Z_{ECEF}/\sqrt{X_{ECEF}^2 + Y_{ECEF}^2}) \quad (A2)$$

and the longitude can be obtained by (range from -180° to 180°)

$$\psi_{GRS} = \begin{cases} -90°, & X = 0, Y < 0 \\ 90°, & X = 0, Y > 0 \\ \tan^{-1}(Y_{ECEF}/X_{ECEF}), & X > 0 \\ \tan^{-1}(Y_{ECEF}/X_{ECEF}) + 180°, & X < 0, Y \leq 0 \\ \tan^{-1}(Y_{ECEF}/X_{ECEF}) - 180°, & X \langle 0, Y \rangle 0 \end{cases} \quad (A3)$$

and the height can be obtained by

$$h = \sqrt{X_{ECEF}^2 + Y_{ECEF}^2 + Z_{ECEF}^2} - N_E. \quad (A4)$$

The transformation between the GCRS and SCRS requires only the translation of the coordinate. For example, if the coordinates in the SCRS are known, the location in the GCRS can be represented by

$$\begin{bmatrix} X_{GCRS} \\ Y_{GCRS} \\ Z_{GCRS} \end{bmatrix} = \begin{bmatrix} X_{SCRS} \\ Y_{SCRS} \\ Z_{SCRS} \end{bmatrix} + \begin{bmatrix} X_{moon} \\ Y_{moon} \\ Z_{moon} \end{bmatrix} \quad (A5)$$

where $\begin{bmatrix} X_{moon} & Y_{moon} & Z_{moon} \end{bmatrix}^T$ is the Moon's position vector in the GCRS, which can be obtained from lunar ephemeris. We used the DE430 ephemeris of Jet Propulsion Laboratory (JPL) in this study.

The transformation between the celestial reference system and the earth-fixed coordinate system requires multiple coordinate system rotations. There are some differences in the rotation matrix between the Earth and Moon. For Earth, the transformation can be expressed as [46], [47]

$$\begin{bmatrix} X_{GCRS} \\ Y_{GCRS} \\ Z_{GCRS} \end{bmatrix} = [M][N][P][E] \begin{bmatrix} X_{ECEF} \\ Y_{ECEF} \\ Z_{ECEF} \end{bmatrix} \quad (A6)$$

where $[M]$, $[N]$, $[P]$, and $[E]$ are the rotation matrices that can be derived by considering Earth's pole motion, nutation, precession, and rotation, respectively. These matrices are time-dependent and can be obtained using the Earth orientation parameters provided by IERS. For Moon, this transformation is performed by [16]

$$\begin{bmatrix} X_{SCRS} \\ Y_{SCRS} \\ Z_{SCRS} \end{bmatrix} = [R_Z][R_X][R_Z] \begin{bmatrix} X_{MCMF} \\ Y_{MCMF} \\ Z_{MCMF} \end{bmatrix} \quad (A7)$$

where $[R_X]$ and $[R_Z]$ represent the rotation matrices around the z-, y-, and z-axes, respectively. The specific rotation angle is related to the lunar libration, which can be obtained from JPL ephemeris.

The transformation between the ECEF and ENU requires coordinate system rotation and translation. The rotation matrices are related to the longitude and latitude of the station. The transformation can be expressed as

$$\begin{bmatrix} E \\ N \\ U \end{bmatrix} = \begin{bmatrix} -\sin\lambda & \cos\lambda & 0 \\ -\sin\varphi\cos\lambda & -\sin\varphi\sin\lambda & \cos\varphi \\ \cos\varphi\cos\lambda & \cos\varphi\sin\lambda & \sin\varphi \end{bmatrix} \begin{bmatrix} X_{ECEF} \\ Y_{ECEF} \\ Z_{ECEF} \end{bmatrix}$$
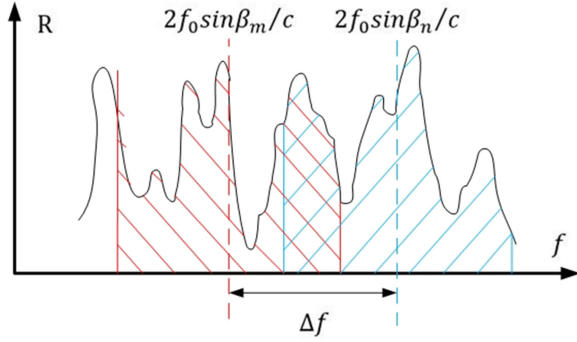$$\begin{bmatrix} 0 \\ 0 \\ H_0 \end{bmatrix} \quad (A8)$$

Fig. 15.   Echo spectrum schematic diagram related to the ground information of the two images.

where λ and φ represent the longitude and latitude of the station. H_0 represents the distance between the station and Earth's center.

APPENDIX B
EFFECTIVE INTERFERENCE SCREENING

InSAR technology needs to be used to perform interference processing on two SAR images with different IAs in the same area, whether it is a dual-antenna system or a single-antenna system with repeat-pass mode. If two SAR images are recorded as S_m and S_n respectively, and the IAs are recorded as β_m and β_n respectively, the echo spectrum movement of these images is different because of the difference in IAs. The spectrum related to the ground information of the two images can be represented by Fig. 15.

The echo of InSAR can be understood as being composed of three parts of the spectrum: exclusive for image S_m, exclusive for image S_n, common for image S_m, and image S_n. The common part of red and blue can affect the coherence of the images, and the size of the common part can be determined by the difference between the two spectrum shifts, which is recorded as Δf

$$
\begin{aligned}
\Delta f &= (\sin\beta_m - \sin\beta_n) \cdot 2f_0/c \\
&= 2\cos\beta\sin\left((\beta_m - \beta_n)/2\right) \cdot 2f_0/c \\
&\approx (\beta_m - \beta_n) \cdot 2f_0\cos\beta/c \\
&\approx B_\perp \cdot 2f_0\cos\beta/(c \cdot S_0) \qquad \text{(A9)}
\end{aligned}
$$

where $B_\perp$ is the vertical baseline, S_0 is the slant range, β is the average of IAs, and $\beta = (\beta_m + \beta_n)/2$. The preconditions for the twice approximation of formula A9 include: $B_\perp \ll S_0$, $(\beta_m - \beta_n)/2 \approx \sin((\beta_m - \beta_n)/2)$ and $(\beta_m - \beta_n) \approx B_\perp/S_0$. When the vertical baseline length increases, such that the movement corresponds to the entire signal bandwidth which can be represented by $2(f_{\max} - f_{\min})\sin\beta/c$, the overlapping part disappears, which is equivalent to the complete loss of the coherent signal. LEO SAR defines the vertical baseline as the critical baseline

$$
B_c = S_0 (f_{\max} - f_{\min})\tan\beta/f_0. \qquad \text{(A10)}
$$

The orbital eccentricity of the moon-based SAR, it is approximately 0.0549, which is 400 times that of LEO SAR. If the

effective interference is screened by the critical baseline, the change in slant range introduces an additional error because the assumptions in A9 are no longer strictly valid. Therefore, this study used the angle relationship to screen for effective interference.

REFERENCES

[1] B. Neil, "Electromagnetic wave propagation, radiation, and scattering: From fundamentals to applications [book review]," *IEEE Antennas Propag. Mag.*, vol. 62, no. 2, pp. 120–121, Apr. 2020.
[2] F. Meyer, K. Chotoo, S. Chotoo, B. Huxtable, and C. Carrano, "The influence of equatorial scintillation on L-Band SAR image quality and phase," *IEEE Trans. Geosci. Remote Sens.*, vol. 54, no. 2, pp. 869–880, Feb. 2016.
[3] A. Ferretti, A. Monti-Guarnieri, C. Prati, F. Rocca, and D. Massonet, "InSAR principles: Guidelines for SAR interferometry processing and interpretation," ESA, TM-19, 2007.
[4] T. Wright, B. Parsons, P. England, and E. Fielding, "InSAR observations of low slip rates on the major faults of western Tibet," *Science*, vol. 305, pp. 236–239, 2004.
[5] Z. Lu, C. Wicks, J. A. Power, and D. Dzurisin, "Ground deformation associated with the March 1996 earthquake swarm at Akutan volcano, Alaska, revealed by satellite radar interferometry," *J. Geophys. Res., Solid Earth*, vol. 105, pp. 21483–21495, 2000.
[6] Z. Shen et al., "Slip maxima at fault junctions and rupturing of barriers during the 2008 Wenchuan earthquake," *Nature Geosci.*, vol. 2, pp. 718–724, 2009.
[7] E. Ramsey, Z. Lu, A. Rangoonwala, and R. Rykhus, "Multiple baseline radar interferometry applied to coastal land cover classification and change analyses," *GISci. Remote Sens.*, vol. 43, pp. 283–309, 2006.
[8] J. Hao et al., "Investigation of a small landslide in the Qinghai-Tibet Plateau by InSAR and absolute deformation model," *Remote Sens. (Basel, Switzerland)*, vol. 11, 2019, Art. no. 2126.
[9] Z. Huang, G. Zhang, X. Shan, W. Gong, Y. Zhang, and Y. Li, "Co-seismic deformation and fault slip model of the 2017 MW 7.3 Darbandikhan, Iran-Iraq earthquake inferred from D-InSAR measurements," *Remote Sens.*, vol. 11, 2019, Art. no. 2521.
[10] K. Wu, C. Ji, L. Luo, and X. Wang, "Simulation study of moon-based InSAR observation for solid earth tides," *Remote Sens.*, vol. 12, 2020, Art. no. 123.
[11] N. Murray et al., "The global distribution and trajectory of tidal flats," *Nature*, vol. 565, pp. 222–225, 2019.
[12] E. Rignot, J. Mouginot, and B. Scheuchl, "Ice flow of the Antarctic ice sheet," *Science*, vol. 333, pp. 1427–1430, 2011.
[13] H. Guo, Y. Ding, G. Liu, W. Fu, and L. Zhang, "Conceptual study of lunar-based SAR for global change monitoring," *Sci. China. Earth Sci.*, vol. 57, pp. 1771–1779, 2014.
[14] J. Dong et al., "An analysis of spatiotemporal baseline and effective spatial coverage for lunar-based SAR repeat-track interferometry," *IEEE J. Sel. Topics Appl. Earth Observ. Remote Sens.*, vol. 12, no. 9, pp. 3458–3469, Sep. 2019.
[15] H. Guo, G. Liu, and Y. Ding, "Moon-based Earth observation: Scientific concept and potential applications," *Int. J. Digit. Earth*, vol. 11, pp. 546–557, 2018.
[16] H. Ye, H. Guo, G. Liu, and Y. Ren, "Observation scope and spatial coverage analysis for earth observation from a Moon-Based platform," *Int. J. Remote Sens.*, vol. 39, pp. 5809–5833, 2018.
[17] M. Calamia, G. Fornaro, G. Franceschetti, F. Lombardini, and A. Mori, "A radar eye on the moon: Potentials and limitations for earth imaging," *PIERS Online*, vol. 6, pp. 330–334, 2010.

[18] Z. Xu, K. S. Chen, P. Xu, and H. Guo, "Ionospheric effects on the lunar-based radar imaging," in *Proc. IEEE Int. Geosci. Remote Sens. Symp.*, 2017, pp. 5390–5393.

[19] W. Zhu, X. L. Ding, H. Jung, and Q. Zhang, "Mitigation of ionospheric phase delay error for SAR interferometry: An application of FR-based and azimuth offset methods," *Remote Sens. Lett.*, vol. 8, pp. 58–67, 2017.

[20] G. Gomba, A. Parizzi, F. D. Zan, M. Eineder, and R. Bamler, "Toward operational compensation of ionospheric effects in SAR interferograms: The split-spectrum method," *IEEE Trans. Geosci. Remote Sens.*, vol. 54, no. 3, pp. 1446–1461, Mar. 2016.

[21] J. Chen and H. A. Zebker, "Ionospheric artifacts in simultaneous L-band InSAR and GPS observations," *IEEE Trans. Geosci. Remote Sens.*, vol. 50, no. 4, pp. 1227–1239, Apr. 2012.

[22] X. Pi, A. Freeman, B. Chapman, P. Rosen, and Z. Li, "Imaging ionospheric inhomogeneities using spaceborne synthetic aperture radar," *J. Geophys. Res., Space Phys.*, vol. 116, 2011, Art. no. A4.

[23] R. Brcic, A. Parizzi, M. Eineder, R. Bamler, and F. Meyer, "Estimation and compensation of ionospheric delay for SAR interferometry," in *Proc. IEEE Int. Geosci. Remote Sens. Symp.*, 2010, pp. 2908–2911.

[24] E. Rignot, "Effect of Faraday rotation on L-band interferometric and polarimetric synthetic-aperture radar data," *IEEE Trans. Geosci. Remote Sens.*, vol. 38, no. 1, pp. 383–390, Jan. 2000.

[25] S. Urban and P. Seidelmann, *Explanatory Supplement to the Astronomical Almanac*, 3rd ed. *American Astronomical Society Meeting*, Sausalito, CA, USA: Univ. Sci. Books 2014.

[26] J. Simon, P. Bretagnon, J. Chapront, M. Chapront-Touze, G. Francou, and J. Laskar, "Numerical expressions for precession formulae and mean elements for the Moon and the planets," *Astron. Astro-Phys.*, vol. 282, pp. 663–683, 1994.

[27] Z. Xu, K. Chen, G. Liu, and H. Guo, "Spatiotemporal coverage of a moon-based synthetic aperture radar: Theoretical analyses and numerical simulations," *IEEE Trans. Geosci. Remote Sens.*, vol. 58, no. 12, pp. 8735–8750, Dec. 2020.

[28] J. Chen, G. Sun, M. Xing, J. Yang, Z. Li, and G. Jing, "A two-dimensional beam-steering method to simultaneously consider doppler centroid and ground observation in GEOSAR," *IEEE J. Sel. Topics Appl. Earth Observ. Remote Sens.*, vol. 10, no. 1, pp. 161–167, Jan. 2017.

[29] T. Long, X. Dong, C. Hu, and T. Zeng, "A new method of zero-Doppler centroid control in GEO SAR," *IEEE Geosci. Remote Sens. Lett.*, vol. 8, no. 3, pp. 512–516, May 2011.

[30] J. Dong et al., "Spatio-temporal distribution of the zero-Doppler line of lunar-based SAR," *Remote Sens. Lett.*, vol. 12, pp. 113–121, 2021.

[31] F. J. Meyer and D. T. Sandwell, "SAR interferometry at Venus for topography and change detection," *Planet. Space Sci.*, vol. 73, pp. 130–144, 2012.

[32] Y. He, "Modeling of InSAR ionospheric delay correction," Chang'an Univ., Xi'an, China, 2019.

[33] Y. Zhou, W. Yun, Q. Xue-Jun, F. Y. Zhu, and Y. Jian, "Anomalous variations of ionospheric VTEC before Ms8.0 Wenchuan earthquake," *Chin. J. Geophys.*, vol. 53, pp. 556–566, 2010.

[34] F. Arikan, S. Shukurov, H. Tuna, O. Arikan, and T. L. Gulyaeva, "Performance of GPS slant total electron content and IRI-Plas-STEC for days with ionospheric disturbance," *Geodesy Geodyn.*, vol. 7, pp. 1–10, 2016.

[35] B. Zhang, J. Ou, Y. Yuan, and Z. Li, "Calibration of slant total electron content and satellite-receiver's differential code biases with uncombined precise point positioning technique," *Acta Geodaetica et Cartographica Sinica*, vol. 40, pp. 447–453, 2011.

[36] Y. Wang, Z. Ding, P. Xu, K. Chen, T. Zeng, and T. Long, "Strip layering diagram-based optimum continuously varying pulse interval sequence design for extremely high-resolution spaceborne sliding spotlight SAR," *IEEE Trans. Geosci. Remote Sens.*, vol. 59, no. 8, pp. 6751–6770, Aug. 2021.

[37] Z. Xu and K. S. Chen, "On signal modeling of moon-based synthetic aperture radar (SAR) imaging of earth," *Remote Sens.*, vol. 10, 2018, Art. no. 486.

[38] C. Hu, J. Hu, X. Dong, and Y. Li, "Analysis of the impacts of ionospheric scintillation on geosynchronous SAR based on spherical wave correction," in *Proc. IEEE Int. Symp. Electromagn. Compat., Asia-Pacific Symp. Electromagn. Compat.*, 2018, pp. 1126–1131.

[39] G. Fornaro, G. Franceschetti, F. Lombardini, A. Mori, and M. Calamia, "Potentials and limitations of Moon-Borne SAR imaging," *IEEE Trans. Geosci. Remote Sens.*, vol. 48, no. 7, pp. 3009–3019, Jul. 2010.

[40] G. Gu, "Vertical crustal movement obtained from GPS observation in China's mainland," *Earthquake*, vol. 25, pp. 1–8, 2005.

[41] G. Kaufmann and K. Lambeck, "Implications of late Pleistocene glaciation of the Tibetan Plateau for present-day uplift rates and gravity anomalies," *Quaternary Res.*, vol. 48, pp. 269–279, 1997.

[42] K. Wu, C. Ji, L. Luo, and X. Wang, "Comprehensive analysis of wide-area observation development for solid earth tides by space technology," *J. Remote Sens.*, 2021, doi: 10.11834/jrs.20210553.

[43] S. Kim and K. Papathanassiou, "SAR observation of ionosphere using range/azimuth sub-bands," in *Proc. IEEE 10th Eur. Conf. Synthetic Aperture Radar*, 2014, pp. 1–4.

[44] J. Hyung-Sup, L. Dong-Taek, L. Zhong, and W. Joong-Sun, "Ionospheric correction of SAR interferograms by multiple-aperture interferometry," *IEEE Trans. Geosci. Remote Sens.*, vol. 51, no. 5, pp. 3191–3199, May 2013.

[45] Y. Sui, H. Guo, G. Liu, and Y. Ren, "Analysis of long-term moon-based observation characteristics for Arctic and Antarctic," *Remote Sens.*, vol. 11, 2019, Art. no. 2805.

[46] Y. Ren, H. Guo, G. Liu, and H. Ye, "Simulation study of geometric characteristics and coverage for moon-based earth observation in the electro-optical region," *IEEE J. Sel. Topics Appl. Earth Observ. Remote Sens.*, vol. 10, no. 6, pp. 2431–2440, Jun. 2017.

[47] H. Ye, H. Guo, G. Liu, and Y. Ren, "Observation duration analysis for Earth surface features from a Moon-Based platform," *Adv. Space Res.*, vol. 62, pp. 274–287, 2018.
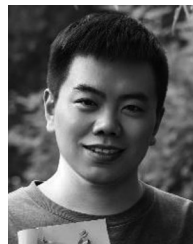
Kai Wu received the B.S. degree in surveying and mapping engineering from the China University of Mining & Techno-logy, Beijing (CUMTB), China, in 2016, and the Ph.D. degree in cartography and geographical information system from the Aerospace Information Research Institute, Chinese Academy of Sciences (CAS), Beijing, China, 2021.

Since 2021, he has been a Postdoctoral Researcher with Aerospace Information Research Institute, CAS. His research interests include moon-based synthetic aperture radar platform, imaging focusing, interferometry simulation, and solid earth deformation inversion.

Huadong Guo (Member, IEEE) received the B.S. degree in geology from the Geology Department, Nanjing University, Nanjing, China, in 1977, and the M.S. degree in geographic information system from the University of Chinese Academy of Sciences (CAS), Beijing, China, in 1981.

He was a Project Leader for more than ten keyprograms related to Earth observation. For the past ten years and at present, he has been one of the principal investigators for SIR-C/X-SAR, JERS-1 SAR, ERS-1/2 SAR, Radarsat-1/2, ENVISAT, SRTM, and ALOS programs. From 1996 to 2000, he was the Principal Scientist with the Expert Group for Information Acquisition and Processing Technology, National High-Tech Research and Development Program in China. He is a Guest Professor with several universities in China. He has authored or coauthored more than 200 articles and 17 books.

Mr. Guo was a recipient of three national awards on science and technology and nine awards by the CAS. He is a member of the International SAR Working Group and the CoDATA Executive Committee, the Chairman of theAssociate on Environment Remote Sensing of China, the Secretary General of the International Society for Digital Earth, and the Editor-in-Chief of the *International Journal of Digital Earth*.

Guang Liu (Member, IEEE) received the B.S. and M.S. degrees in physics from Tsinghua University, Beijing, China, in 1999 and 2002, respectively, and the Ph.D. degree in geographic information system from the Institute of Remote Sensing Applications, Chinese Academy of Sciences (CAS), Beijing, China, in 2008.

From 2006 to 2007, he was a Guest Researcher with Mathematical Geodesy and Positioning, Delft University of Technology, Delft, The Netherlands. In 2008, he joined the Institute of Remote Sensing and Digital Earth, CAS. His work was focused on the Moon-based Earth observation studies and near real-time ground motion monitoring using synthetic aperture radar (SAR) satellite. He has authored more than 40 lead authored peer-reviewed JCR journal articles. He is a PI of ESA CAT-1, DRAGON-3, DRAGON-4, and DLR AO projects, and five national-funded projects.

Yixing Ding received the B.S. and M.S. degrees in geographical information science from Wuhan University, Wuhan, China, in 2005 and 2007 respectively, and the Ph.D. degree in signal and information processing from University of Chinese Academy of Sciences, Beijing, China, in 2014.

He is a Research Associate with Aerospace Information Research Institute, Chinese Academy of Sciences, and International Research Center of Big Data for Sustainable Development Goals. His current research interests include Moon-based Earth observation, high resolution remote sensing, and remote sensing for natural disasters.

Wenjin Wu received the B.E. degree in remote sensing science and technology from Wuhan University, Wuhan, China, in 2010 and the Ph.D. degree in cartography and geography information system from the Institute of Remote Sensing and Digital Earth, Chinese Academy of Sciences (CAS), Beijing, China, in 2015.

She is currently an Associate Professor of Aerospace Information Research Institute. CAS and the author of more than 60 academic papers. Her research interests include big data analysis, deep learning, and high-resolution SAR data information extraction.

Guoqiang Chen received the B.S. degree in electrical engineering and automation from Yangtze University, Jingzhou, China, in 2014, and the M.S. degree in traffic information engineering & control from Beijing Jiaotong University, Beijing, China, in 2018. He is currently working toward the Ph.D. degree in cartography and geographical information system from Aerospace Information Research Institute, Chinese Academy of Sciences, Beijing, China, and from the University of Chinese Academy of Science.

His current research interest focuses on the Moon-based Earth observation.